Research Article | Vol. 8, No. 4 | 1 Apr 2017 | BIOMEDICAL OPTICS EXPRESS 2287

Biomedical Optics EXPRESS

# Handheld optical coherence tomography angiography

**JIANLONG YANG, LIANG LIU, J. PETER CAMPBELL, DAVID HUANG, AND GANGJUN LIU***

*Casey Eye Institute, Oregon Health and Science University, 3375 SW Terwilliger Blvd, Portland, OR 97239, USA*

**liga@ohsu.edu*

**Abstract:** We developed a handheld optical coherence tomography angiography (OCTA) system using a 100-kHz swept-source laser. The handheld probe weighs 0.4 kg and measures 20.6 × 12.8 × 4.6 $cm^3$. The system has dedicated features for handheld operation. The probe is equipped with a mini iris camera for easy alignment. Real-time display of the *en face* OCT and cross-sectional OCT images in the system allows accurately locating the imaging target. Fast automatic focusing was achieved by an electrically tunable lens controlled by a golden-section search algorithm. An extended axial imaging range of 6 mm allows easy alignment. A registration algorithm using cross-correlation to register adjacent OCT B-frames with propagation from the central frame was used to effectively minimize motion artifacts in volumetric OCTA images captured in relatively short durations of 1 and 2.1 seconds. 2.5 × 2.5 mm (200 × 200 pixels) and 3.5 × 3.5 mm (300 × 300 pixels) retinal angiograms were demonstrated on two awake adult human subjects without the use of any mydriatic eye drops.



**OCIS codes:** (110.4500) Optical coherence tomography; (170.4460) Ophthalmic optics and devices; (170.3880) Medical and biological imaging.

## References and links

1. D. Huang, E. A. Swanson, C. P. Lin, J. S. Schuman, W. G. Stinson, W. Chang, M. R. Hee, T. Flotte, K. Gregory, C. A. Puliafito, and J. G. Fujimoto, "Optical coherence tomography," Science **254**(5035), 1178–1181 (1991).
2. G. J. Jaffe, and J. Caprioli, "Optical coherence tomography to detect and manage retinal disease and glaucoma," Am. J. Ophthalmol. **137**(1), 156–169 (2004).
3. C. K. Leung, C. Y. Cheung, R. N. Weinreb, Q. Qiu, S. Liu, H. Li, G. Xu, N. Fan, L. Huang, C. P. Pang, and D. S. Lam, "Retinal nerve fiber layer imaging with spectral-domain optical coherence tomography: a variability and diagnostic performance study," Ophthalmology **116**(7), 1257–1263, 1263.e1–1263.e2 (2009).
4. R. K. Wang, S. L. Jacques, Z. Ma, S. Hurst, S. R. Hanson, and A. Gruber, "Three dimensional optical angiography," Opt. Express **15**(7), 4083–4097 (2007).
5. G. Liu, A. J. Lin, B. J. Tromberg, and Z. Chen, "A comparison of Doppler optical coherence tomography methods," Biomed. Opt. Express **3**(10), 2669–2680 (2012).
6. S. S. Gao, Y. Jia, M. Zhang, J. P. Su, G. Liu, T. S. Hwang, S. T. Bailey, and D. Huang, "Optical coherence tomography angiography," Invest. Ophthalmol. Vis. Sci. **57**(9), OCT27–OCT36 (2016).
7. R. F. Spaide, J. M. Klancnik, Jr., and M. J. Cooney, "Retinal vascular layers imaged by fluorescein angiography and optical coherence tomography angiography," JAMA Ophthalmol. **133**(1), 45–50 (2015).
8. T. E. de Carlo, A. Romano, N. K. Waheed, and J. S. Duker, "A review of optical coherence tomography angiography (OCTA)," Int J Retina Vitreous **1**(1), 5 (2015).
9. A. Ishibazawa, T. Nagaoka, A. Takahashi, T. Omae, T. Tani, K. Sogawa, H. Yokota, and A. Yoshida, "Optical coherence tomography angiography in diabetic retinopathy: a prospective pilot study," Am. J. Ophthalmol. **160**(1), 35–44.e1 (2015).
10. L. Liu, Y. Jia, H. L. Takusagawa, A. D. Pechauer, B. Edmunds, L. Lombardi, E. Davis, J. C. Morrison, and D. Huang, "Optical coherence tomography angiography of the peripapillary retina in glaucoma," JAMA Ophthalmol. **133**(9), 1045–1052 (2015).
11. Y. Jia, S. T. Bailey, D. J. Wilson, O. Tan, M. L. Klein, C. J. Flaxel, B. Potsaid, J. J. Liu, C. D. Lu, M. F. Kraus, J. G. Fujimoto, and D. Huang, "Quantitative optical coherence tomography angiography of choroidal neovascularization in age-related macular degeneration," Ophthalmology **121**(7), 1435–1444 (2014).
12. A. W. Scott, S. Farsiu, L. B. Enyedi, D. K. Wallace, and C. A. Toth, "Imaging the infant retina with a hand-held spectral-domain optical coherence tomography device," Am. J. Ophthalmol. **147**(2), 364–373.e2 (2009).
13. W. Jung, J. Kim, M. Jeon, E. J. Chaney, C. N. Stewart, and S. A. Boppart, "Handheld optical coherence tomography scanner for primary care diagnostics," IEEE Trans. Biomed. Eng. **58**(3), 741–744 (2011).

#282470 https://doi.org/10.1364/BOE.8.002287
Journal © 2017 Received 8 Dec 2016; revised 25 Feb 2017; accepted 12 Mar 2017; published 22 Mar 2017

Biomedical Optics EXPRESS


14. S. I. Sayegh, R. M. Nolan, W. Jung, J. Kim, D. T. McCormick, E. J. Chaney, C. N. Stewart, and S. A. Boppart, "Comparison of a MEMS-based handheld OCT scanner with a commercial desktop OCT system for retinal evaluation," Transl. Vis. Sci. Technol. **3**(3), 10 (2014).
15. C. D. Lu, M. F. Kraus, B. Potsaid, J. J. Liu, W. Choi, V. Jayaraman, A. E. Cable, J. Hornegger, J. S. Duker, and J. G. Fujimoto, "Handheld ultrahigh speed swept source optical coherence tomography instrument using a MEMS scanning mirror," Biomed. Opt. Express **5**(1), 293–311 (2014).
16. F. LaRocca, D. Nankivil, S. Farsiu, and J. A. Izatt, "Handheld simultaneous scanning laser ophthalmoscopy and optical coherence tomography system," Biomed. Opt. Express **4**(11), 2307–2321 (2013).
17. F. LaRocca, D. Nankivil, S. Farsiu, and J. A. Izatt, "True color scanning laser ophthalmoscopy and optical coherence tomography handheld probe," Biomed. Opt. Express **5**(9), 3204–3216 (2014).
18. F. LaRocca, D. Nankivil, T. DuBose, A. Cynthia Toth, S. Farsiu, and J. A. Izatt, "In vivo cellular-resolution retinal imaging in infants and children using an ultracompact handheld probe," Nat. Photonics **10**(9), 580–584 (2016).
19. G. Liu, Y. Jia, A. D. Pechauer, R. Chandwani, and D. Huang, "Split-spectrum phase-gradient optical coherence tomography angiography," Biomed. Opt. Express **7**(8), 2943–2954 (2016).
20. Z. Wang, H.-C. Lee, O. O. Ahsen, B. Lee, W. Choi, B. Potsaid, J. Liu, V. Jayaraman, A. Cable, M. F. Kraus, K. Liang, J. Hornegger, and J. G. Fujimoto, "Depth-encoded all-fiber swept source polarization sensitive OCT," Biomed. Opt. Express **5**(9), 2931–2949 (2014).
21. American National Standard Institute (ANSI). American National Standard for the Safe Use of Lasers (2000).
22. J. P. Su, Y. Li, M. Tang, L. Liu, A. D. Pechauer, D. Huang, and G. Liu, "Imaging the anterior eye with dynamic-focus swept-source optical coherence tomography," J. Biomed. Opt. **20**(12), 126002 (2015).
23. K. Aljasem, A. Werber, A. Seifert, and H. Zappe, "Fiber optic tunable probe for endoscopic optical coherence tomography," J. Opt. A, Pure Appl. Opt. **10**(4), 044012 (2008).
24. J. Kiefer, "Sequential minimax search for a maximum," Proc. Am. Math. Soc. **4**(3), 502–506 (1953).
25. W. H. Press, S. A. Teukolsky, W. T. Vetterling, and B. P. Flannery, Numerical Recipes: The Art of Scientific Computing (3rd ed.), New York: Cambridge University Press (2007).
26. S. Ricco, M. Chen, H. Ishikawa, G. Wollstein, and J. Schuman, "Correcting motion artifacts in retinal spectral domain optical coherence tomography via image registration," Med Image Comput Comput Assist Interv **12**(Pt 1), 100–107 (2009).
27. T. M. Jørgensen and B. Sander, "Contrast enhancement of retinal B-scans from OCT3/Stratus by image registration—clinical application," Proc. SPIE **6426**, 642608 (2007).
28. M. F. Kraus, B. Potsaid, M. A. Mayer, R. Bock, B. Baumann, J. J. Liu, J. Hornegger, and J. G. Fujimoto, "Motion correction in optical coherence tomography volumes on a per A-scan basis using orthogonal scan patterns," Biomed. Opt. Express **3**(6), 1182–1199 (2012).
29. P. Zang, G. Liu, M. Zhang, C. Dongye, J. Wang, A. D. Pechauer, T. S. Hwang, D. J. Wilson, D. Huang, D. Li, and Y. Jia, "Automated motion correction using parallel-strip registration for wide-field en face OCT angiogram," Biomed. Opt. Express **7**(7), 2823–2836 (2016).
30. S. S. Gao, G. Liu, D. Huang, and Y. Jia, "Optimization of the split-spectrum amplitude-decorrelation angiography algorithm on a spectral optical coherence tomography system," Opt. Lett. **40**(10), 2305–2308 (2015).
31. M. Guizar-Sicairos, S. T. Thurman, and J. R. Fienup, "Efficient subpixel image registration algorithms," Opt. Lett. **33**(2), 156–158 (2008).
32. R. J. Zawadzki, A. R. Fuller, S. S. Choi, D. F. Wiley, B. Hamann, and J. S. Werner, "Correction of motion artifacts and scanning beam distortions in 3D ophthalmic optical coherence tomography imaging," Proc. SPIE **6426**, 642607 (2007).
33. B. Antony, M. D. Abràmoff, L. Tang, W. D. Ramdas, J. R. Vingerling, N. M. Jansonius, K. Lee, Y. H. Kwon, M. Sonka, and M. K. Garvin, "Automated 3-D method for the correction of axial artifacts in spectral-domain optical coherence tomography images," Biomed. Opt. Express **2**(8), 2403–2416 (2011).
34. M. D. Abràmoff, M. K. Garvin, and M. Sonka, "Retinal Imaging and Image analysis," IEEE Rev. Biomed. Eng. **3**, 169–208 (2010).
35. K. Li, X. Wu, D. Z. Chen, and M. Sonka, "Optimal surface segmentation in volumetric images--a graph-theoretic approach," IEEE Trans. Pattern Anal. Mach. Intell. **28**(1), 119–134 (2006).
36. M. K. Garvin, M. D. Abramoff, R. Kardon, S. R. Russell, X. Wu, and M. Sonka, "Intraretinal layer segmentation of macular optical coherence tomography images using optimal 3-D graph search," IEEE Trans. Med. Imaging **27**(10), 1495–1505 (2008).
37. K. Li, X. Wu, D. Z. Chen, and M. Sonka, "System and Methods for Image segmentation in N- dimensional space" US Patent 7,995,810.
38. G. Liu, O. Tan, S. S. Gao, A. D. Pechauer, B. Lee, C. D. Lu, J. G. Fujimoto, and D. Huang, "Postprocessing algorithms to minimize fixed-pattern artifact and reduce trigger jitter in swept source optical coherence tomography," Opt. Express **23**(8), 9824–9834 (2015).
39. T. Klein, W. Wieser, L. Reznicek, A. Neubauer, A. Kampik, and R. Huber, "Multi-MHz retinal OCT," Biomed. Opt. Express **4**(10), 1890–1908 (2013).
40. I. Grulkowski, J. J. Liu, B. Potsaid, V. Jayaraman, C. D. Lu, J. Jiang, A. E. Cable, J. S. Duker, and J. G. Fujimoto, "Retinal, anterior segment and full eye imaging using ultrahigh speed swept source OCT with vertical-cavity surface emitting lasers," Biomed. Opt. Express **3**(11), 2733–2751 (2012).

Biomedical Optics EXPRESS

41. J. P. Su, R. Chandwani, S. S. Gao, A. D. Pechauer, M. Zhang, J. Wang, Y. Jia, D. Huang, and G. Liu, "Calibration of optical coherence tomography angiography with a microfluidic chip," J. Biomed. Opt. **21**(8), 086015 (2016).

## 1. Introduction

Optical coherence tomography (OCT) is a noninvasive imaging technique that can achieve *in vivo* high-resolution cross-sectional images of the human eye and has been widely used in the diagnosis and treatment of various diseases in ophthalmology such as glaucoma, diabetic retinopathy, and age-related macular degeneration (AMD) [1–3]. By comparing the difference (intensity, phase or both) between two successive OCT B-scans (with a time interval of several milliseconds) at the same location, an OCT technique known as OCT Angiography (OCTA) can further characterize the vasculature and blood flow in the human retina [4–6]. Compared with traditional fluorescein angiography (FA) and indocyanine green angiography (ICGA), OCTA diminishes the risk of the side effects of dye injection and minimizes the time consumption [7]. Besides, it also provides useful volumetric information of the retinal vasculature. In recent years, OCTA has become a commercially available tool in ophthalmology to detect vascular change such as capillary density dropout or pathologic vessel growth in diabetic retinopathy and AMD [8–11].

Most of the commercial and research OCT systems for ophthalmology are in a fix-mounted table-top form, which requires the research subjects or patients sit in front of the machine and hold their eye open for several seconds to finish the imaging process. This is difficult for people with certain types of disabilities and young children. To improve the portability and application coverage of the OCT system, different kinds of handheld OCT probes in the forms of prototype and commercial product have been developed for research and clinical applications in recent years. In 2009, Scott *et al.* have evaluated the infant retina through the use of a hand-held spectral-domain optical coherence tomography (SD OCT) device in selected cases of Shaken Baby syndrome [12]. In 2011, Jung *et al.* demonstrated a handheld OCT scanner to image the cross-sectional and 3D images of human eye based on SD OCT technique [13]. Then they improved their probe by substituting the galvo scanning mirrors with a microelectromechanical (MEMS) scanning mirror, which makes the handheld probe more compact and lighter [14]. In 2013, Lu *et al.* used swept source (SS) OCT technique and MEMS to build handheld OCT probes. Wide-field *en face* images (10 × 10 $mm^2$) of the human retina were retrieved from the handheld OCT instrument [15]. Besides, a series of research works on the development of handheld scanning laser ophthalmoscopy (SLO) and OCT probe have demonstrated by researchers at Duke University [16,17]. Most recently, they observed the retinal photoreceptor cells of young children based on their well-developed handheld probe and SLO imaging technique [18]. Compared to conventional structure OCT and SLO, the OCTA bases the contrast on the red blood cell movement, which is more sensitive to motion artifacts. OCTA is preferred to be visualized from the *en face* plane and a 3D volume has to be acquired to generate the *en face* OCTA. In addition, OCTA algorithms require repeated B-scans at the same location to calculate the flow contrast. All of these requirements make the successful acquisition of OCTA from a handheld device very challenging.

In this paper, we developed a handheld OCT system with features optimized for OCTA applications, which include a golden search based fast automatic focusing subsystem, an extended axial imaging range, fast scanning protocols and a simple registration algorithm. Based on a recently-developed high-efficient OCTA algorithm, split-spectrum amplitude phase-gradient angiography (SSAPGA) [19], we demonstrate retina OCTA images from healthy awake volunteers with acquisition times of 1 second and 2.1 seconds.

Biomedical Optics EXPRESS

## 2. Methods

### *2.1 Extended axial imaging range 1050-nm swept source OCT system*

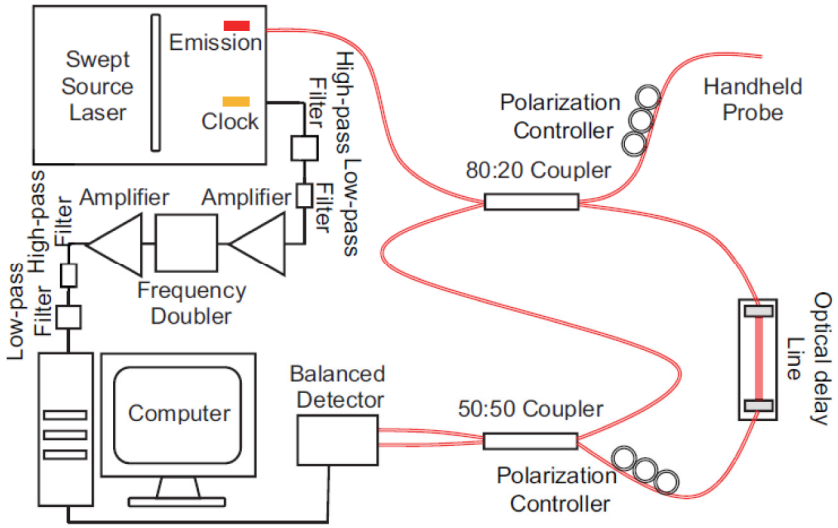


Fig. 1. The configuration of the 1050-nm swept-source OCT system.

The schematic of the 1050-nm SS-OCT system is shown in Fig. 1. The laser source is a swept laser (Axsun 1060, Axsun Technologies, Billerica, MA, USA) with a repetition rate (A-line speed) of 100 kHz, a central wavelength of 1050 nm and a tuning range of 110 nm, giving a theoretical axial resolution of ~5.7 μm. An 80/20 fiber coupler (AC Photonics, Santa Clara, CA, USA) is used to split the laser from the source into the sample arm (20%) and reference arm (80%). The light of the sample arm then goes into the handheld OCTA probe as illustrated in Fig. 1. An optical delay line (ODL-100, OZ Optics, Ottawa, ON, Canada) and single-mode fibers are used to match the path length in both arms. The light scattered/back-reflected by the sample and the light of the reference arm goes through a 50/50 coupler (TW1064R5F2A, Thorlabs, Newton, NJ, USA) and finally into a balanced detector (PDB471C, Thorlabs, Newton, NJ, USA) with a bandwidth from DC to 400 MHz. The detected signal is collected by a data acquisition board (ATS9350, AlazarTech, Pointe-Claire, QC, Canada) with a sampling rate up to 500 MS/s and a resolution of 12 bits.

With the built-in k-clock from the laser source, the SS-OCT system has an axial imaging range of ~3 mm in tissue. This range is enough for benchtop OCT systems. However, we found that, for the handheld OCTA system, a longer axial imaging range is preferred because of the involuntary motions induced by both the operator and the patient. To solve this problem, we adopted a frequency doubling circuit [20] to double the k-clock frequency and increase axial imaging range. The k-clock signal output from the laser source was filtered with a high-pass (ZX75LP-340-S + , Minicircuit, Brooklyn, NY, USA) and a low-pass filter (SHP-200 + , Minicircuit, Brooklyn, NY, USA). The signal was then amplified by a power amplifier (ZFL-1000 + , Minicircuit, Brooklyn, NY, USA). The amplified signal then went through a frequency doubler (MK-2, Minicircuit, Brooklyn, NY, USA). The frequency doubled signal was filtered (ZX75LP-900-S + &SHP-400 + , Minicircuit, Brooklyn, NY, USA) and amplified again (ZRL-700 + , Minicircuit, Brooklyn, NY, USA) and served as the k-clock of data acquisition. This method increases the imaging range to 6 mm and greatly reduce the image cropping artifact during the capture process (demonstrated in Section 3.1).

Biomedical Optics EXPRESS

### 2.2 Handheld OCTA probe

Figure 2(a) shows the optical setup of the handheld OCTA probe. The light from the sample arm was transmitted through a single-mode fiber. The laser beam then passed through a collimator, an electronically tunable lens (EL-10-30-C, Optotune, Dietikon, Switzerland) and a two-axes galvometer scanner (GVS002, Thorlabs, Newton, NJ, USA). A telescope was used as the imaging optics. The scan lens and ocular lens are pairs of achromatic doublets (AC254-050-B&AC254-030-B, Thorlabs, Newton, NJ, USA) with focus lengths of 50 mm and 30 mm, respectively. The working distance for the probe is ~14 mm. The optics above enables an FWHM beam size of 2 mm on the cornea, which was measured by a scanning slit optical beam profiler (BP209-IR, Thorlabs, Newton, NJ, USA). The theoretical transverse resolution is 10 μm on the retina and the actual lateral resolution may be worse due to the aberration of the eye. The laser power entering the pupil is 1.85 mW, which is within the laser safety limits according to the ANSI Z136.1 standard [21]. A micro USB borescope endoscope (Sokos Borescope, Amazon, Seattle, WA, USA) is used as an iris camera for easy alignment. It has a resolution of 640 × 480 pixels. The camera comes with six LEDs for illumination and the brightness of the LEDs are tunable. The whole camera has a diameter of 7 mm including the illumination LEDs. As illustrated in the figure, we use an off-axis design of the camera to reduce the system complexity and the size of the probe. The controlling software could display the summed voxel projection (*SVP*) OCT image processed in real-time and the operator can pick the region to be imaged based on the *SVP* OCT image.

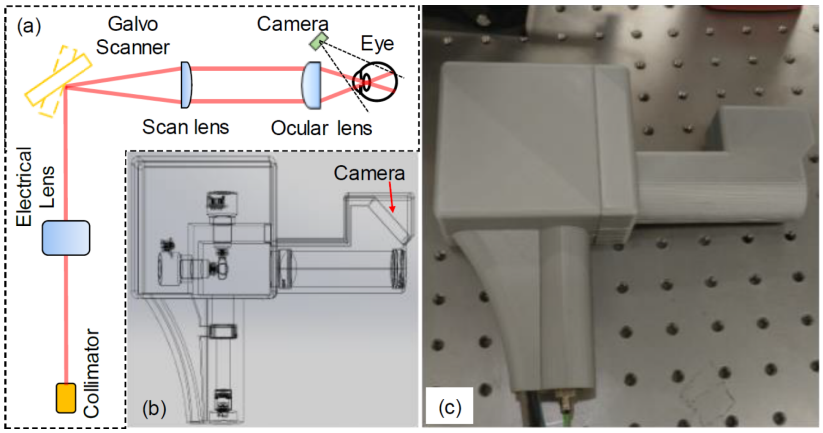


Fig. 2. (a) Schematic of the handheld OCTA probe. (b) 3-dimensional (3D) perspective view of the probe including all the optical components and the designed plastic case for mounting and holding. (c) Photograph of the handheld OCTA probe with 3D-printed enclosure.

Figure 2(b) is the 3-dimensional (3D) perspective view of the probe including all the optical components and the designed plastic case for mounting and holding. Figure 2(c) is the photography of the handheld OCTA probe. We fabricated the silver color plastic enclosure of the probe by a 3D printer (Ultimaker 2 + , Ultimaker B.V., Geldermalsen, Netherlands). The finished probe has the dimensions of 20.6 × 12.8 × 4.6 $cm^3$ and a weight of 0.4 kg.

Biomedical Optics EXPRESS

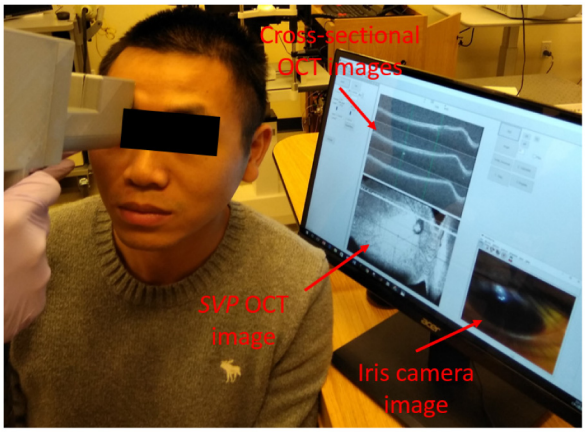


Fig. 3. The photograph shows the imaging a volunteer with the handheld OCTA system. The iris camera image is used for initial alignment for find the pupil. After that, summed-voxel projection OCT and the cross-sectional OCT images are used to guide the operation.

Figure 3 is a photograph that demonstrates a moment of the imaging process by the handheld OCTA probe. The human study protocol was approved by the Oregon Heath & Science University Institutional Review Board and followed the tenets of the Declaration of Helsinki in the treatment of human subjects. As demonstrated in the figure, real-time iris image, *SVP* OCT, and cross-sectional images were displayed for alignment. The iris camera is used for initial fast locating of the pupil. Once the pupil is found, and the operator will be mainly guided by the real-time *SVP* and cross-sectional OCT images. The *SVP* OCT preview image has a field of view of ~11 mm by11 mm and is updated at 4 frames per second. The operator could choose and change the targeted imaging area location and size based on the *SVP* OCT preview image. The eye fixation was realized by staring at specific locations under the guidance of the operator. No pupil dilation required for the handheld OCTA imaging process. To further optimize the capture process, we developed an automatic focusing method (described in Section 2.3) and increased the axial imaging range for avoiding image cropping (described in Section 2.4 and 3.1).

### *2.3 Golden-section search based automatic focus tuning*

For handheld OCT systems, manually focusing tuning mechanisms have been demonstrated [13–18]. The manual focusing procedure is slow, and usually, the results are not ideal because the operator has to, subjectively, decide if the image is in focus or not. Translational stages have been used for automatic focus in commercial OCT systems. However, they are usually bulky and slow, so they are not suitable for handheld OCT system. We have demonstrated a dynamic focusing system based on an electrical lens [22]. The lens has a fast response time of ~5 ms. This fast response time of the lens could allow a fast automatic procedure. In addition, an advanced searching algorithm which does not require continuous tuning of the lens can be used for automatic focusing. In this study, we included an electrical lens in the handheld OCTA probe, which not only simplifies the system design but also reduces the time needed for automatic focusing. These features are very important for handheld OCT device. It is well-known that the OCT reflectance is a unimodal function of focal plane position and the maximum OCT reflectance value is obtained when the sample is located at the focal plane [23]. Thus the search for the optimum focal plane becomes an extremum search problem of a unimodal function. All the extremum search algorithms such as binary search and Fibonacci search can also be used for this purpose. Here, we used the golden section search algorithm for its high efficiency and robustness [24,25]. This method successively narrows the range of values inside which the extremum is known to exist.

Biomedical Optics EXPRESS

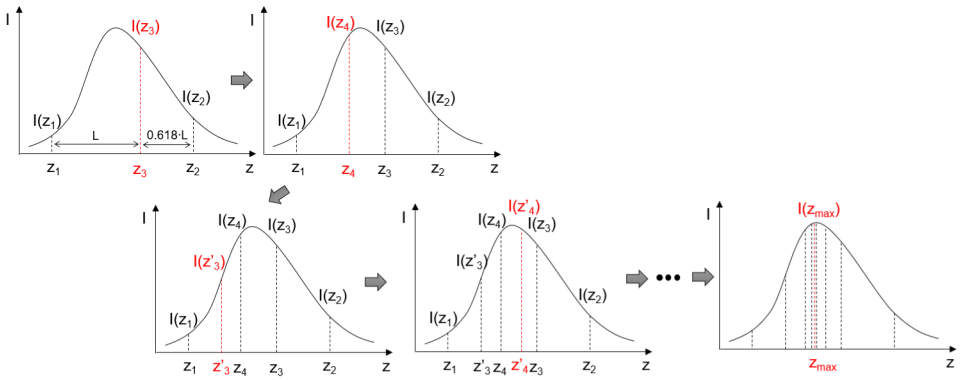


Fig. 4. The golden section search algorithm for automatic focus tuning. $z_1$ and $z_2$ are the two initial boundaries of the search region. Two extra intensities ( $I(z_3)$ *and* $I(z_4)$ ) at the golden ratio distance from the initial boundaries are then calculated based on the intensities at the two boundaries. The search region is narrowed down by comparing $I(z_2)$ and $I(z_4)$. The boundaries of the search region are updated according to the values at $z_3$ and $z_4$ . The values of $z_3$ and $z_4$ are then the replaced by the values of $z_3'$ and $z_4'$ accordingly. This process is repeated until the difference between $I(z_2)$ and $I(z_4)$ is smaller than a pre-defined threshold.

Figure 4 is a graphic illustration of the golden section search algorithm. The software provides a button to initialize the auto-focus procedure. Once started, the software repeats scanning at the central B-scan location of the targeted imaging area. The number of pixels with intensity of more than a threshold of OCT is used as a parameter (signal strength index) to represent the brightness of the image (*I* in Fig. 4). $z$ in Fig. 4 is a variable representing different focal planes of the electric lens and $z_1$ and $z_2$ are the two initial boundaries of the search region. Each z in Fig. 4 is corresponding to a control current for the electrical lens. The searching for optimized focal plane location is the same as searching for the maximum of all the *I*. To achieve this, the intensities at the two search boundaries: $I(z_1)$ and $I(z_2)$ are obtained firstly. Two new focal plane positions $z_3$ and $z_4$ are then calculated according to:

$$z_3 = z_1 + 0.618(z_2 - z_1), \tag{1}$$

$$z_4 = z_2 + 0.618(z_1 - z_2). \tag{2}$$

The intensities at the two new positions: $I(z_3)$ and $I(z_4)$ are then obtained. The search region is then narrowed down by comparing the values of $I(z_3)$ and $I(z_4)$ . If $I(z_3) - I(z_4) < \varepsilon$ , where $\varepsilon$ is a pre-defined threshold, the search is done and the location for maximum intensity can be calculated as $z_{max} = (z_3 + z_4)/2$ . Otherwise, if $I(z_3) < I(z_4)$ , the search region is narrowed down to $[z_1, z_3]$. If $I(z_3) > I(z_4)$ , the search region is narrowed down to $[z_4, z_2]$. The new boundaries of the search region are used to update the values of $z_3$ , $z_4$ to $z_3'$ , $z_4'$ and their intensities. This search region narrowing process is repeated until the criteria $|I(z_3) - I(z_4)| < \varepsilon$ is met.

Biomedical Optics EXPRESS

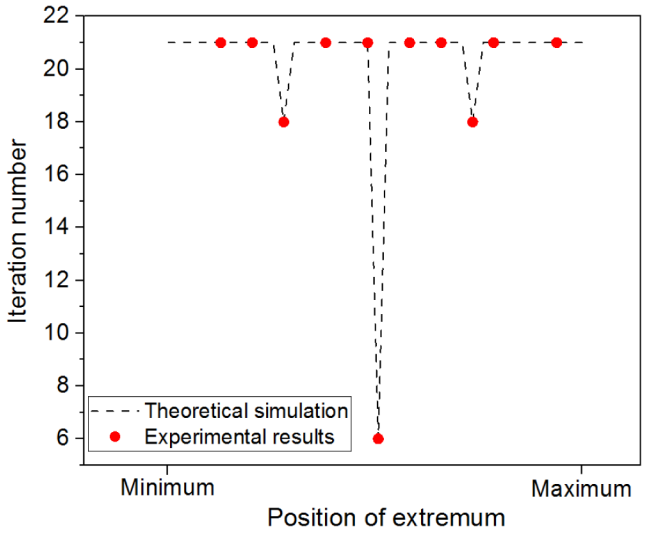


Fig. 5. Iteration numbers required in the automatic focus tuning process. The black dash-line was from theoretical simulation based on the golden section search algorithm, and the red dots were the measured results from two experiments. The maximum and majority of the iteration numbers is 21.

To demonstrate the performance of the golden section search algorithm for the automatic focusing in OCT, experimental verifications were performed. In one experiment, a 60D lens (Volk Optical Inc., Mentor, OH) was used to focus the light from the handheld OCT and an infrared detector card (VRC5, Thorlabs Inc, Newton, New Jersey) was used as a sample. The infrared detector card was mounted on a translational stage so that the distance between the 60D lens and the card can be tuned. By changing the card from around zero optical path delay (ZOPD) of the OCT system to 6mm away from the ZOPD with a step of 0.5mm, we calculated the iteration numbers of the golden section search algorithm for each step. The results of the golden section search were verified by manual changing the current and then checking the signal strength index (brightness) of the OCT images. In another experiment, the 60D lens and another electrical focus tunable lens (EL-6-18, Optotune, Dietikon, Switzerland) were combined together to focus the light on the infrared detector card which located at the 3mm away from the ZOPD of the system. By changing the current for the focus tunable lens with a 50 mA step, we calculated the iteration numbers of the golden section search algorithm again. It was found that the maximum (and majority) of the iteration numbers were 21. There were also a few iteration numbers which were 6 or 18. A Matlab-based theoretical simulation was also performed. In the simulation, a Gaussian shape distribution was assumed for the OCT reflectance changing with defocusing. The peak of the Gaussian shape is always located within the search region. By changing the location of the peak of the Gaussian profile, we calculated the number of iteration for the golden section search algorithm. Figure 5 shows the simulation results as well as the experimental results. Both theory and experiment results show the majority (the maximum also) of the iteration numbers are 21. In the automatic focus mode, each B-scan OCT image contains 256 A-lines and the total time to acquire these images is ~100 milliseconds.

### *2.4 Fast 1 second and 2.1 seconds OCTA scanning protocols*

Motion artifact, especially micro-saccades, is the main challenge for OCTA, which is based on motion contrast. Typical OCTA system requires 3~4 seconds to capture one OCTA volume if no eye-tracking module is used. To correct the motion artifact, an eye tracking system could be used, which will increase the system complexity and cost. Another way to

Biomedical Optics EXPRESS

correct the motion artifact in based on post-processing methods, which usually require multiple volumetric data sets [26–28]. For a handheld system, we would expect more motion artifacts because the motions will be from both the patient and operator. Here, to reduce the motion artifact, we will reduce the imaging time. We will demonstrate OCTA imaging with 1 second and 2.1 seconds imaging time for a field of view of 2.5 × 2.5 mm and 3.5 × 3.5 mm, which will significantly reduce the effect of motion artifacts. To reduce the imaging time, we used only two repeated B-scan modes at the same location. Two different scan protocol with 1 second and 2.1 seconds imaging time were tested. In the first protocol, an area of 2.5 × 2.5 $mm^2$ (200 × 200 pixels) was captured in 1 second. In this mode, two repeated B-scans at the same location with 250 A-lines per B-scan (50 data points for galvanometer fly-back) was used, and a total of 400 B-scans was acquired in a 3D OCT volume. The time separation between the B-scans at the same location is 2.5 ms, and the total scan duration is 1 second. In the second protocol, an area of 3.5 × 3.5 $mm^2$ (300 × 300 data points) was captured in 2.1 seconds. Two repeated B-scans at the same location with 350 A-lines per B-scan (50 data points for galvanometer fly-back) was used, and a total of 600 B-scans was acquired in a 3D OCT volume for the OCTA calculation. The time separation between the B-scans at the same location is 3.5 ms, and the total scan duration is 2.1 seconds.

### *2.5 Highly efficient OCTA algorithm and propagation-based image registration*

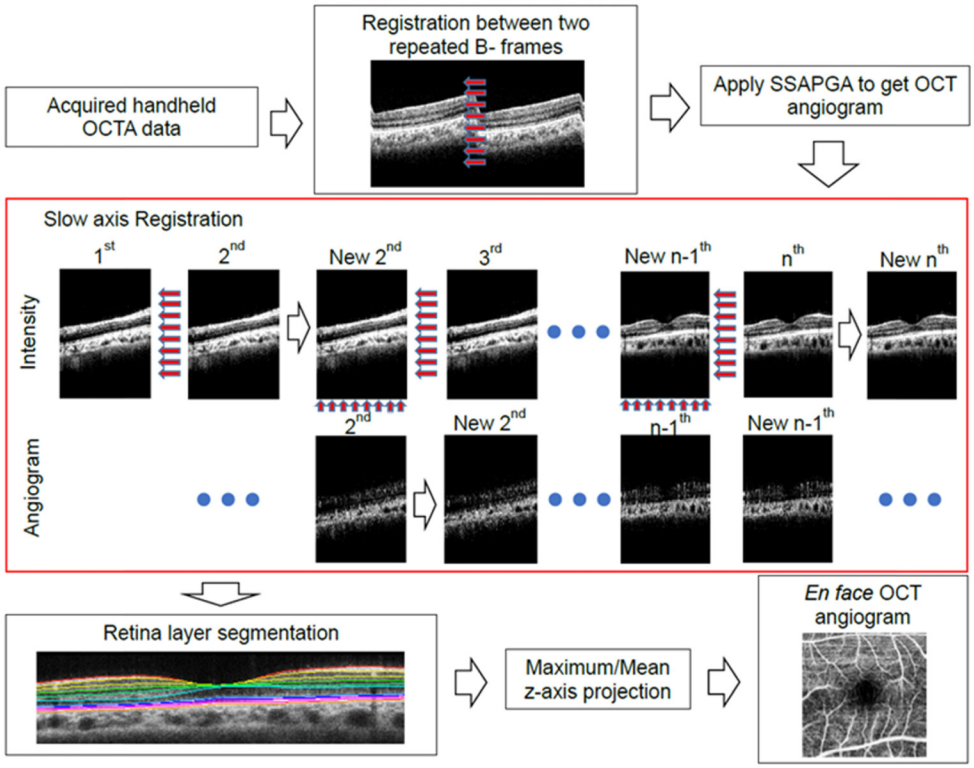


Fig. 6. The processing flowchart for generating *en face* retinal OCTA. A propagation-based OCT image registration algorithm was used to correct the motion artifact as shown in the red box. Registration between adjacent images was propagated from the reference image to all the rest images. The motion corrected image volume was segmented with a 3D graph search segmentation software. *En face* retina OCTA was generated based on the segmentation results.

To obtain high-quality OCTA images with only 2 B-scan repetitions, highly efficient OCTA algorithms have to be used. We have shown that split-spectrum could improve that signal to noise ratio (SNR) and combining both phase and amplitude information could improve the

Biomedical Optics EXPRESS

SNR further [19, 29]. Here, the SSAPGA algorithm is used for calculating the OCTA flow. In Fig. 6, we illustrate the processing flow chart of the data to generate *en face* retinal angiograms. First, registration between two repeated B-frames at the same location was performed using subpixel image registration algorithm introduced in [30]. Then SSAPGA was used to calculate the angiograms. Although the 1 second and 2.1 seconds imaging protocol will reduce the motion artifact, motion artifact can still exist. As demonstrated in the previous researches [15, 28, 30], motion artifact always exists along the slow scan direction. A simple registration algorithm that is similar to the one based on cross-correlation between adjacent OCT B-frames with propagation is used [32]. Here, the B-scan image at the center of the 3D volume is used as a reference and an efficient subpixel image registration algorithm is adopted to register adjacent OCT B-frames [31]. The registration process starts from the reference B-frame and the registered B- frames will serve as a reference to its adjacent B-frames that have not been registered (Fig. 6).

To verify the effectiveness of the registration method, 3D volumetric data captured with two orthogonal scans (x-fast and y-fast) from the same retina location are processed, respectively, with the method. Figure 7 shows the 3D rendering of the volumetric data before [Figs. 7(a), 7(c), 7(e) and 7(g)] and after [Figs. 7(b), 7(d), 7(f) and 7(h)] the registration. Before the registration, both 3D rendering results from the x-fast scan [Fig. 7(a) and 7(e)] and the y-fast scan [Fig. 7(c) and 7(g)] shows eye motion along the slow scan directions. After registration, the profiles of the retinal inner limiting membrane layers and other layers become much smooth and the rendering results from the orthogonal scans show great similarity.

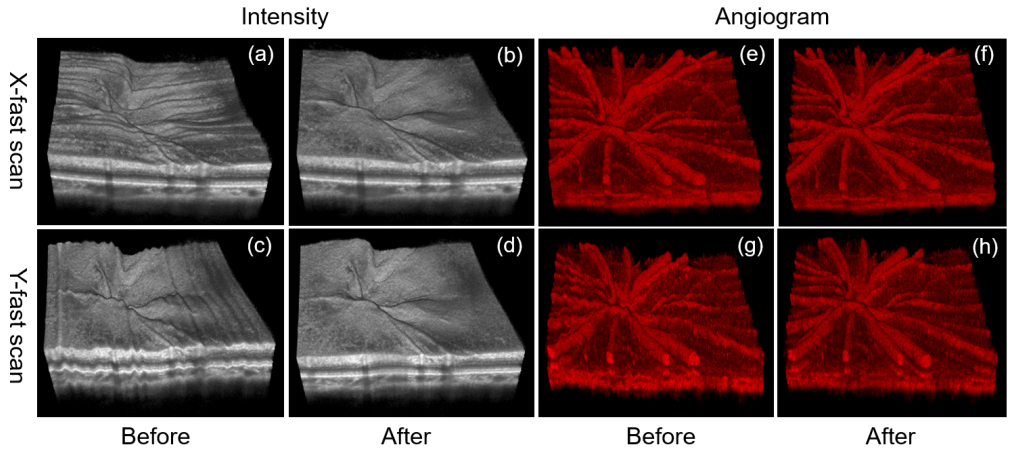


Fig. 7. 3D rendering of retina OCT image set before (a) (c) and after (b) (d) image registration. The results of one x-fast scan (a) (b) and one y-fast scan (c) (d) are employed for comparison. (e), (f), (g) and (h) are OCTA volumes corresponding to (a), (b), (c) and (d).

To further verify that this method recovers the true retinal structure, we compared the cross-sectional slices extracted from the volumes obtained with the two orthogonal scans. Figure 7 demonstrates the comparison of two orthogonal cross-sectional slices before and after the image registration. The locations of the two slices are shown as green and red lines in the registered 3D volume [Fig. 8(a)]. Figures 8(b), 8(c), and 8(d) show the cross-sectional slices extracted from the x-fast volume, the registered x-fast volume, and the registered y-fast volume, respectively. The gray image is the OCT B-scan reflectance and the overlaid red color represents the OCTA. We can find that cross-sectional image [Fig. 8(c)] along the slow scan direction extracted from the registered x-fast volume is much smoother than the one [Fig. 8(b)] extracted from the unregistered x-fast volume. The two cross-section slices along the red line location [Figs. 8(c) and 8(d)] that are extracted from the registered x-fast and the y-fast volumes show great similarity. This shows that the method is effective to recover the

Biomedical Optics EXPRESS

true cross-sectional retinal structure. The cross-sectional slices [Figs. 8(e), 8(f), and 8(g)] along the green line in Fig. 8(a) are extracted from the unregistered y-fast volume, the registered y-fast volume, and the registered x-fast volume, respectively. The similarity between Figs. 8(g) and 7(g), again, proves the effectiveness of this method.

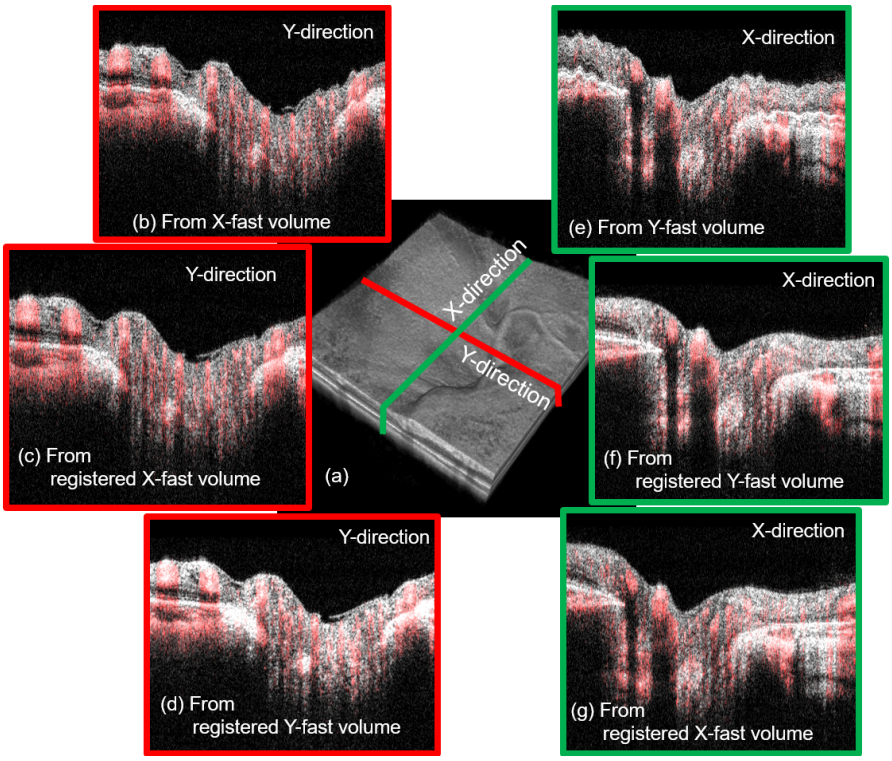


Fig. 8. Comparison of the two orthogonal cross-sectional slices (red and green lines in a) extracted from the registered and unregistered 3D rendering volumes. The gray image is the OCT B-scan reflectance and the overlaid red color represents the OCTA. (a) The 3D rendering result for the registered volume. (b-d) The cross-sectional images along the y direction (red line location in a) extracted from the unregistered x-fast volume, the registered x-fast volume, and the registered y-fast volume. (e-f) The cross-sectional images along the x direction (green line location in a) extracted from the registered y-fast volume, the registered y-fast volume, and the registered x-fast volume.

This registration method is simple, straightforward, and effective for motion correction along the slow-axis scan direction when the scanning size is relative small. It should be noted that this registration method does not correct saccadic motion artifact, which may introduce gap/discontinuity in the image volume. In the case of saccade, merging and averaging of two or more volumetric scans should be used to correct it as demonstrated in the previous OCT registration methods [26–29]. However, this method is helpful when only one imaging volume exists or the registration methods based on multiple volumes fail. After the slow-axis registration, layer segmentation was performed the 3D volume using an automated segmentation tools based on 3D graph search [33–37]. Maximum intensity projection *en face* retinal OCTA was generated based on the segmentation results.

Biomedical Optics EXPRESS

## 3. Results

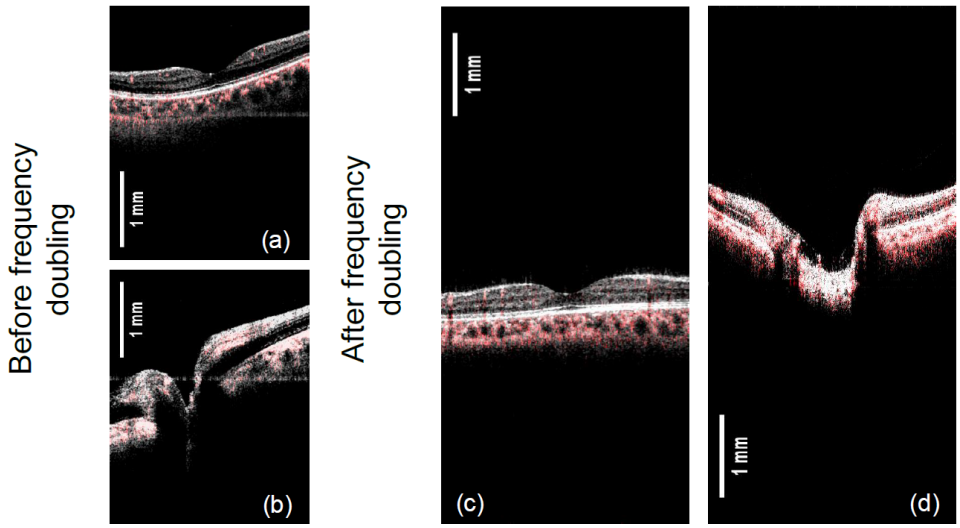


Fig. 9. Demonstration of the axial imaging range before and after the frequency doubling of the k-clock. The gray image is the OCT B-scan intensity and the overlaid red color represents the OCTA.

In Fig. 9, we demonstrate the axial imaging range before and after the frequency doubling of the k-clock. Figures 9(a) and 9(g) show the overlaid intensity and angiographic images obtained with the built-in k-clock provided by the laser source. It can be seen that with the built-in k-clock, the structures of the retina in both fovea and disk regions take up to 50% of the total axial imaging range, which could be further increased for the severe myopic eye. The swept source laser used in this study has trigger jitter/ phase stability issue. The horizontal lines in Figs. 9(a) and 9(b) are the results of the trigger jitter from the swept laser. A typical OCT system has an axial imaging range of less than 3.5mm, this axial imaging range makes the acquisition of high-quality image very challenging. The operator has to control the probe working distance very precisely to keep the retina image in the axial range and avoid image cropping. In addition, the working distance has to be maintained during the image acquisition. A long axial imaging range would greatly relax the requirement. In spectral domain OCT system, a longer axial imaging range is challenging due to system sensitivity roll-off. The sensitivity roll-off performance of the short cavity swept laser has been increased greatly in recent years. The swept laser used in this study has a coherence length of ~12 mm. With the increased axial imaging range to ~6.6 mm by frequency doubling, the system demonstrated a 6dB sensitivity roll-off depth of 6 mm. It was found that using the k-clock with doubled frequency further reduced the phase stability of the system. To solve this, we have developed a post-processing algorithm which reduced the trigger jitter artifact and improved the system phase stability [38]. Figures 9(c) and 9(d) show the OCT images with extended axial imaging range. From Figs. 9(c) and 9(d), it can be found that the images are free from trigger jitter induced line artifact after using the trigger jitter correction algorithm.

Biomedical Optics EXPRESS

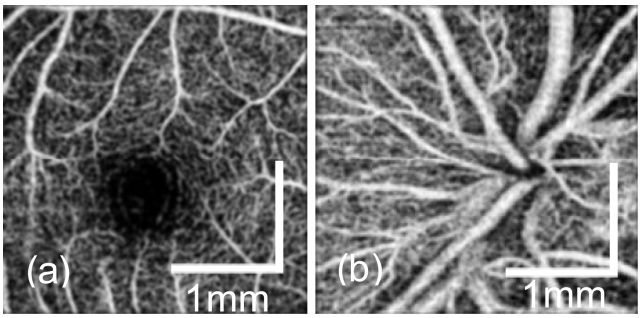


Fig. 10. *En face* retina OCTA around the fovea (a) and ONH (b) from a healthy eye by using the scan protocol 2.5 × 2.5 $mm^2$ (200 × 200 data points).

We demonstrate the *en face* retinal angiogram around the fovea [Fig. 10(a)] and the optical nerve head [Fig. 10(b)] locations for a healthy volunteer. The 1-second scanning protocol was used. The benefits of the fast 1 second imaging time are two folds. Firstly, the motion artifacts from the imaging subject and the operator are greatly reduced. Secondly, a short imaging time enables multiple 3D volumes to be acquired in a short period. The fast 1 second OCTA scan protocol has a sampling step size of 12.5 μm, which is comparable to commercial OCTA system. However, it took only 1 second for the handheld system to acquire the data set so that the motion artifact is greatly reduced. From Fig. 10, it can be seen that the capillaries are clearly visible in the images. By increasing the capturing time, a larger scan area was also demonstrated as shown in Fig. 11. The 2.1-second scan protocol was used. The image has a field of view of 3.5 × 3.5 mm and contains 300 × 300 pixels. As shown in the figure, reasonable-quality angiograms can be achieved with this handheld device. Both large vessels and capillaries are clearly visualized in the images.

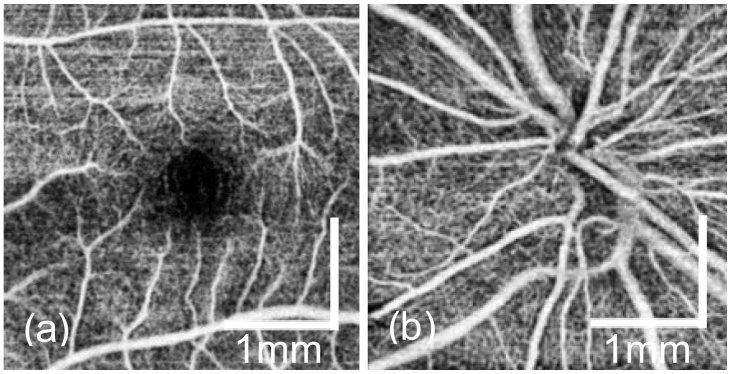


Fig. 11. *En face* OCTA around the fovea (a) and the ONH (b) from a health eye by using the scan protocol 3.5 × 3.5 $mm^2$ (300 × 300 data points).

## 4. Discussion

It is necessary to further discuss its limitations and possible improvements of the current system. First, with a faster swept laser [39], the A-line rate can be increased to megahertz, which will not only further shorten the scan duration but also reduce the involuntary eye motion. Wide field and high dense scans can be realized and multiple successive volumetric scans can be achieved to improve the SNR and correct motion artifacts. With the laser sources of ultra-narrow instantaneous bandwidth, such vertical-cavity surface emitting lasers [40], the axial imaging range can be further increased without sacrificing the system sensitivity. Second, although the registration algorithm could improve 3D rendering, it does not correct saccadic motion artifact, which may introduce gap/discontinuity in the image volume. Fortunately, the very short scan durations we minimize the large motion artifacts. In the case

Biomedical Optics EXPRESS

where micro-saccades do happen, we can employ the motion-correction methods directly using multiple volumes, such as orthogonal registration or parallel-strip registration methods [26–29]. Thirdly, benefited from the compact optical design and 3D-printed plastic enclosure, the probe is light and easy to handle. But it still has room for improvements. For example, the two-axes galvo scanner can be replaced by a MEMS scanner to further decrease the weight and volume of the handheld OCTA probe. However, a further test of the possibility of using MEMS for OCTA is needed.

With the current scanning protocol, the sampling density (11~12.5 μm) is under Nyquist sampling density (~5.0 μm). The current sampling density was similar to the scan modes of commercial OCTA systems (such as AngioVue on Avanti, Optovue Inc and AngioPlex on the CIRRUS 5000 HD, Carl Zeiss Meditec, Inc.), which have been proven to be able to image the capillaries of the human retina. However, the under-sampling will reduce the contrast of the OCTA images [41]. To achieve a sampling density with Nyquist sampling while maintaining the field of view, a faster swept laser or a longer acquisition time is needed. We are in the process of developing a faster system to solve this issue.

## 5. Conclusions

We developed a handheld probe for OCTA applications. We used 3D printing technology for the mounting of the optical components included and the enclosure of the handheld probe. The finished prototype has a weight of 0.4 kg and a dimension of 20.6 × 12.8 × 4.6 $cm^3$. The system has dedicated features designed for handheld applications. These features include an extended axial imaging range, a mini iris camera, an ultrafast automatic focusing system and simple registration method. We demonstrated high-quality OCTA images of undilated normal eyes with the 1-second and 2.1-second scan protocols.

## Financial disclosures

Dr. David Huang has a significant financial interest in Optovue, Inc., a company that may have a commercial interest in the results of this research and technology. Dr. David Huang also has a financial interest in Carl Zeiss Meditec, Inc. These potential conflicts of interest have been reviewed and managed by OHSU. Other authors do not have a financial interest in the subject of this article.

## Funding

This research was funded by Oregon Health and Science Foundation, National Institutes of Health Grants R01 EY023285, R01 EY018184, Lloyd Research Foundation (OHSU), unrestricted departmental funding from Research to Prevent Blindness (New York, NY), and P30 EY010572 from the National Institutes of Health (Bethesda, MD).